Supplementary Materials for

"Mechanical control of electroresistive switching"

Yunseok Kim[1,2], Simon J. Kelly,[1,3] Anna Morozovska,[4] Ehsan Kabiri Rahani,[5] Evgheni Strelcov[1], Eugene Eliseev[6], Stephen Jesse[1], Michael D. Biegalski[1], Nina Balke[1], Nicole Benedek,[7] Dmitri Strukov,[8] J. Aarts[3], Inrok Hwang[9], Sungtaek Oh[9], Jin Sik Choi[9], Taekjib Choi[10], Bae Ho Park[9], Vivek B. Shenoy[11], Peter Maksymovych[1], and Sergei V. Kalinin[1 *]*

[1] The Center for Nanophase Materials Sciences, Oak Ridge National Laboratory, Oak Ridge, Tennessee 37831, USA

[2] School of Advanced Materials Science & Engineering, Sungkyunkwan University, Suwon 440-746, Republic of Korea

[3] Leiden Institute of Physics, Leiden University, Niels Bohrweg 2, 2333 CA Leiden Netherlands

[4] Institute of Physics, National Academy of Science of Ukraine, 46, pr. Nauki, 03028 Kiev, Ukraine

[5] School of Engineering, Brown University, Providence, RI 02906, USA

[6] Institute for Problems of Materials Science, National Academy of Science of Ukraine, 3, Krjijanovskogo, 03142 Kiev, Ukraine

[7] Materials Science and Engineering Program, The University of Texas at Austin, 1 University Station, Austin, TX 78712, USA

[8] Department of Electrical and Computer Engineering, University of California, Santa Barbara, CA 93106, USA

[9] Division of Quantum Phases & Devices, Department of Physics, Konkuk University, Seoul 143-701, Korea

[10] Hybrid Materials Research Center and Department of Nanotechnology and Advanced Materials Engineering, Sejong University, Seoul 143-747, Korea

[11] Department of Materials Science and Engineering, University of Pennsylvania, Philadelphia PA 19104, USA

[*] Address correspondence to yunseokkim@skku.edu; sergei2@ornl.gov

I. Experimental results

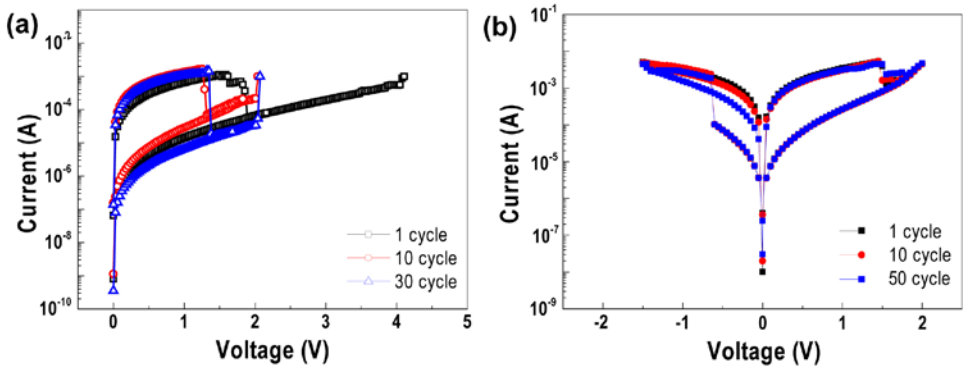

Figure S1. (a) Uni-polar and (b) bi-polar resistive switching of a NiO film.

NiO is well known as a resistive switching material in which electrochemical reactions underpin basic operational mechanisms of resistive switching.[1-4] Shown in Fig. S1 is resistive switching behavior obtained by electrical macroscopic measurements for a Pt/NiO/SRO capacitor. The present films show both uni- and bi-polar switching behavior. The results show repeatable resistive switching behavior implying that the material is controlled by reversible electrochemical reactions.

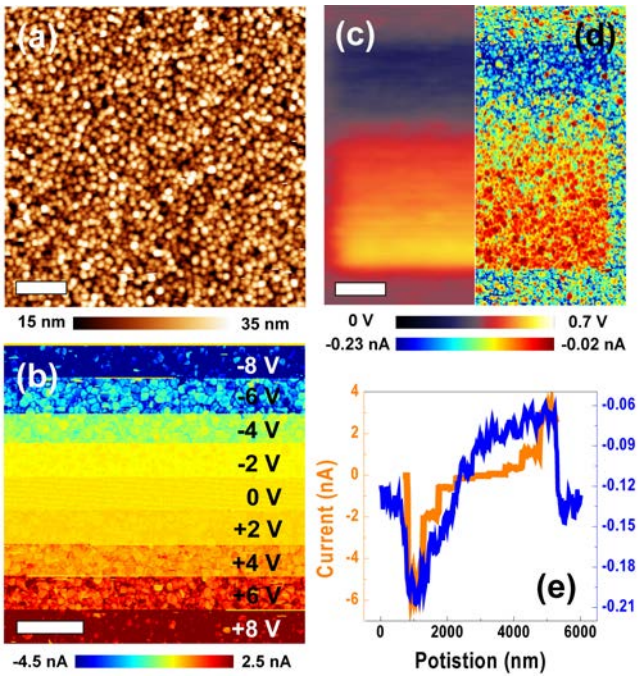

Figure S2. (a) Topography, (b,d) CAFM, and (c) KPFM images of a NiO film (b) during and (a,c,d) after applying bias voltages by diamond coated tips from -8 V to +8 V under the set point of 0.5 V. CAFM image in (d) was taken under -2 V. (e) Average current line profiles from CAFM images. Orange and blue lines are taken from Figs. (b) and (c), respectively. 1.0 V of set point corresponds to about 1500 nN. The scale bar is 1 μm.

The application of positive bias using diamond coated tips leads to positively-charged surface (KPFM) and high-resistance state (CAFM), as similar to Fig. 1 using Pt/Cr coated tips.

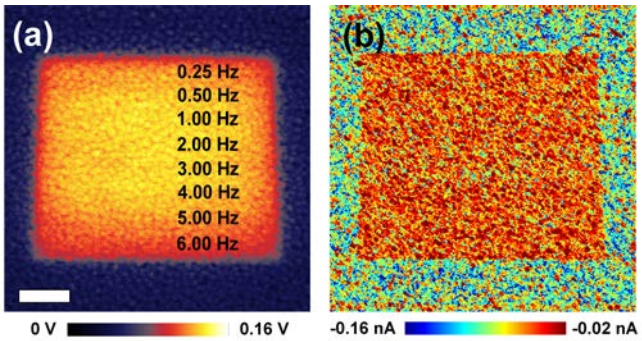

Figure S3. (a) KPFM and (b) CAFM images of a NiO film after scanning with constant scan lines of 64 under different scan speed by Pt/Cr coated tip. CAFM image in (b) was taken under -2 V. The scale bar is 1 μm.

In order to explore triboelectric charge, we compare the changes in surface potential and conductivity under different scanning conditions. We scanned the sample surface under fixed number of scan lines and the scan rate only increases from 0.25 Hz to 6.00 Hz under 64 scan lines. On increasing scan speed for fixed number of lines, it shows the same surface potential and conductivity in everywhere [see Figs. S3(b,c)]. Friction force depends on scan speed under the same contact force. Hence, even though different friction forces are applied to the sample, the surface potential and conductance of the sample are constant in scanned area, which exclude triboelectric effect as a potential origin.

On the other hand, the scanned areas in Fig. S3 show positively increased surface potential compared to the pristine surface. Since the contact electrification[5] induced by the grounded metal coated tip cannot increase toward more positive surface potential,[6] the contact electrification can be excluded as one of possible mechanisms.

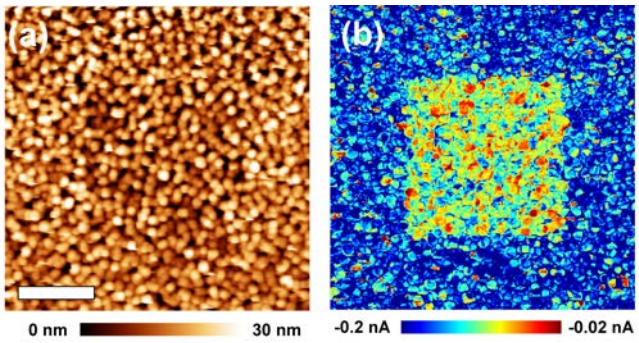

Figure S4. (a) Topography and (b) CAFM images of a NiO film after force-distance grid measurements over an area of 2.0 μm (128 × 128 resolution) with maximum set point of 3.0 V (corresponding to 4.5 μN force exerted by the cantilever) by diamond coated tip. CAFM image was taken under -2 V and set point of 0.5 V. The scale bar is 1 μm.

We further performed force-distance (F-D) grid measurements which allow us applying high set point without scanning the sample surface and, eventually, the friction effect, *i.e.* triboelectricity, can be excluded during the measurements. The measured area clearly shows high-resistance state which is coincident to the result of Fig. 2. Hence, we believe that the piezochemical effect is responsible for the observed phenomena.

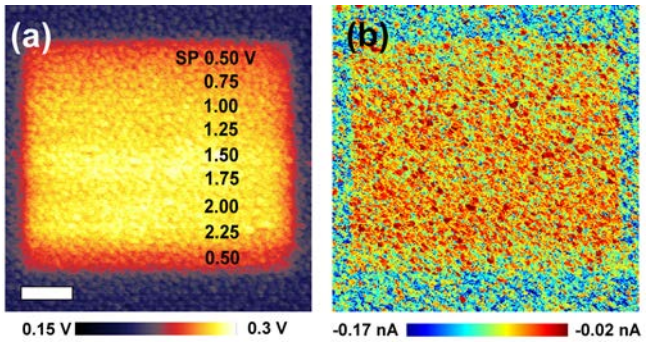

Figure S5. (a) KPFM and (b) CAFM images of a NiO film after scanning with different set point by Pt/Cr coated tip. 1.0 V of set point corresponds to about 80 nN. The scale bar is 1 μm.

On increasing contact force, both surface potential and current show slight change on the signal. The obtained results are similar to those of Fig. 2, but the change is smaller due to the lower contact force which is now strongly affected by capillary forces (constant offset).

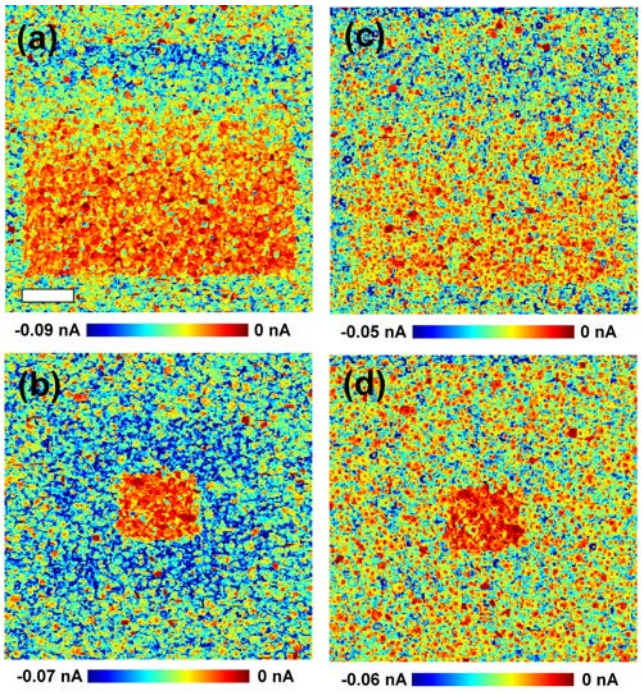

Figure S6. CAFM images of a NiO film under -1 V: (a,c) as-written and (b,d) relaxed images taken about 15 hours after (a,b) applying bias voltage from -8 V to +8V and (c,d) writing background pattern of -6 V and inner pattern of +6 V through diamond coated tip. The scale bar is 1 μm.

We have checked its stability by current mapping under low voltage. Even though current signal partially degrades 15 hours later, we still can observe the box patterns. This indicates that the written conductive states are thermodynamically stable.

II. Theory of piezochemical effect

The contributions of concentration-strain coupling and configuration entropy of the charged species is:[7]

$$F = \int_V d^3r\left(\left(\Xi_{ij}^C\left(n-n_0\right)+\beta_{ij}^d\left(N_d^+ - N_{d0}^+\right)\right)u_{ij} + k_BT\,S\left(n_0,n\right)+k_BT\,S\left(N_{d0}^+,N_d^+\right)\right)+\frac{c_{ijkl}}{2}u_{ij}u_{kl} \quad \text{(Eq. S1)}$$

Linear fit of the data shown in Figure S7 allows us to estimate the values of deformation potential $\Xi_{11}^C = \Xi_{22}^C = \Xi_{33}^C$ in accordance with formula as

$$-\Xi_{11}^C = \frac{\partial E_g\left(u_{11}\right)}{\partial u_{11}} \approx \begin{cases} \dfrac{E_g\left(u_{11}\right)-E_g\left(0\right)}{u_{11}} = \dfrac{3.972-3.872}{0.04} = -1.075\,eV, \quad 0 \le u_{11} \le 0.04, \\ \dfrac{E_g\left(u_{11}\right)-E_g\left(0\right)}{u_{11}} = \dfrac{4.015-3.972}{-0.04} = -2.5\,eV, \quad -0.04 \le u_{11} \le 0. \end{cases} \quad \text{(Eq. S2)}$$

Here u_{11} is the uniaxial elastic strain, $E_g\left(u_{11}\right) = E_V\left(u_{11}\right) - E_C\left(u_{11}\right)$ is the band gap.

Despite the estimated values formally is within the range Ξ_{ij}^C ~(1 - 5) eV, the difference for the negative and positive strains are evident. This is absolutely reasonable, since possible degeneration in the center of BR zone disappears with the strain, and different levels play the major role at positive and negative strains correspondingly.[8]

In the Boltzmann-Planck-Nernst approximation, the configuration entropy function is $S(x,y) = y\ln(y/x) - y$, where T is the absolute temperature. Equation S1 includes electrochemical concentration-deformation energy $\left(\Xi_{ij}^C\left(n-n_0\right)+\beta_{ij}^d\left(N_d^+ - N_{d0}^+\right)\right)u_{ij}$ which is determined by the convolution of the tensorial deformation potential tensor Ξ_{ij}^C and Vegard expansion tensor β_{ij}^d with elastic strain tensor $u_{jk}(\mathbf{r})$. In the absence of external potential, flexoelectric coupling and strains, the equilibrium concentrations of the electrons in the conduction band and ionized defects are represented as n_0 and N_{d0}^+, respectively. Variation of the energy (Eq. S1) with respect to the strain $\partial F/\partial u_{ij} = \sigma_{ij}$ and concentrations n and N_d^+

gives corresponding equation between them, such as $N_d^+ \approx N_{d0}^+ \exp\left(\left(\beta_{ij}^d \delta u_{ij} - e f_{ij33} \delta u_{ij} - e\varphi_{ext}\right)/k_B T\right)$. Solid red curve in Figure S8 improves phenomenological electronic plot using more complex dependence as

$$n = n_0 \exp\left(\frac{\partial E_C\left(u_{11}\right)}{\partial u_{11}} \frac{\delta u_{ij}}{k_B T} + e\frac{\delta\varphi_{flexo}}{k_B T}\right) \quad \text{(Eq. S3)}$$

where $\delta\varphi_{flexo} = f_{ij33}\delta u_{ij}$, instead of the dependence shown by dashed curves in Figure S8:

$$n = n_0 \exp\left(\left(\Xi_d^C \delta u_{ii} + e\delta\varphi_{flexo} + e\varphi_{ext}\right)/k_B T\right), \quad \text{(Eq. S4)}$$

where Ξ_{ij}^C was regarded constant within the range (1 - 5) eV. Also valence band can be shifted for the holes in the similar way, *e.g.* $p = p_0 \exp\left(\frac{\partial E_V\left(u_{11}\right)}{\partial u_{11}} \frac{\delta u_{ij}}{k_B T} - e\frac{\delta\varphi_{flexo}}{k_B T}\right)$. Electrostatic potential term $e\delta\varphi_{flexo} = e f_{mn33}\delta u_{mn}$ appears n and N_d^+ after inclusion of the electrostatic energy and flexoelectric energy (Lifshitz invariant) into Eq. (S1).

With typical parameters (for NiO) and universal constants: the absolute temperature of T = 300 K, e=1.6×10^{-19} C, and Kogan estimation for the flexoelectric effect, coefficient give f_{ijkl} ~5 V (*i.e.* $e f_{ij33}$ ~5 eV), deformation potential Ξ_{ij}^C ~1.075 eV, Vegard stress coefficient β_{ij}^d = 2, 10, and 20 eV, strain $u_{ij} \sim 0.01 - 0.001$, $s_{ii} = 5\times10^{-12}$ Pa^{-1}, $\varphi_{ext} = 0$, and $\sigma_{ij} \sim 10^9$ Pa, respectively.

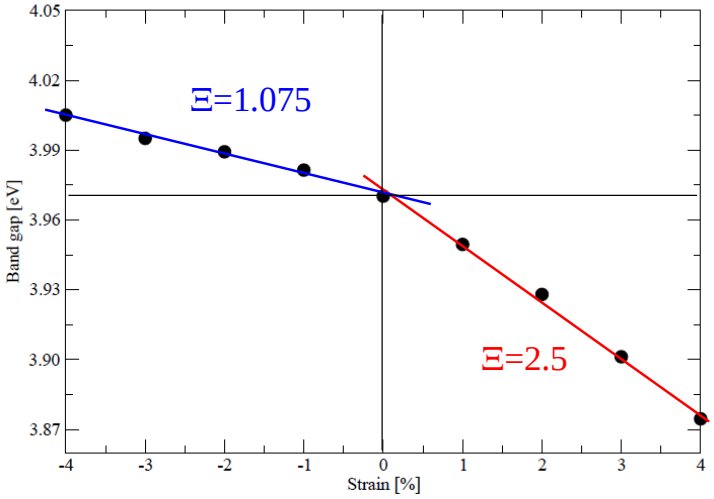

Figure S7. Change in NiO band gap as a function of C_{11} strain from DFT-LSDA+U calculations. Note that negative (posivive) values of strain denote compressive (tensile) strain.

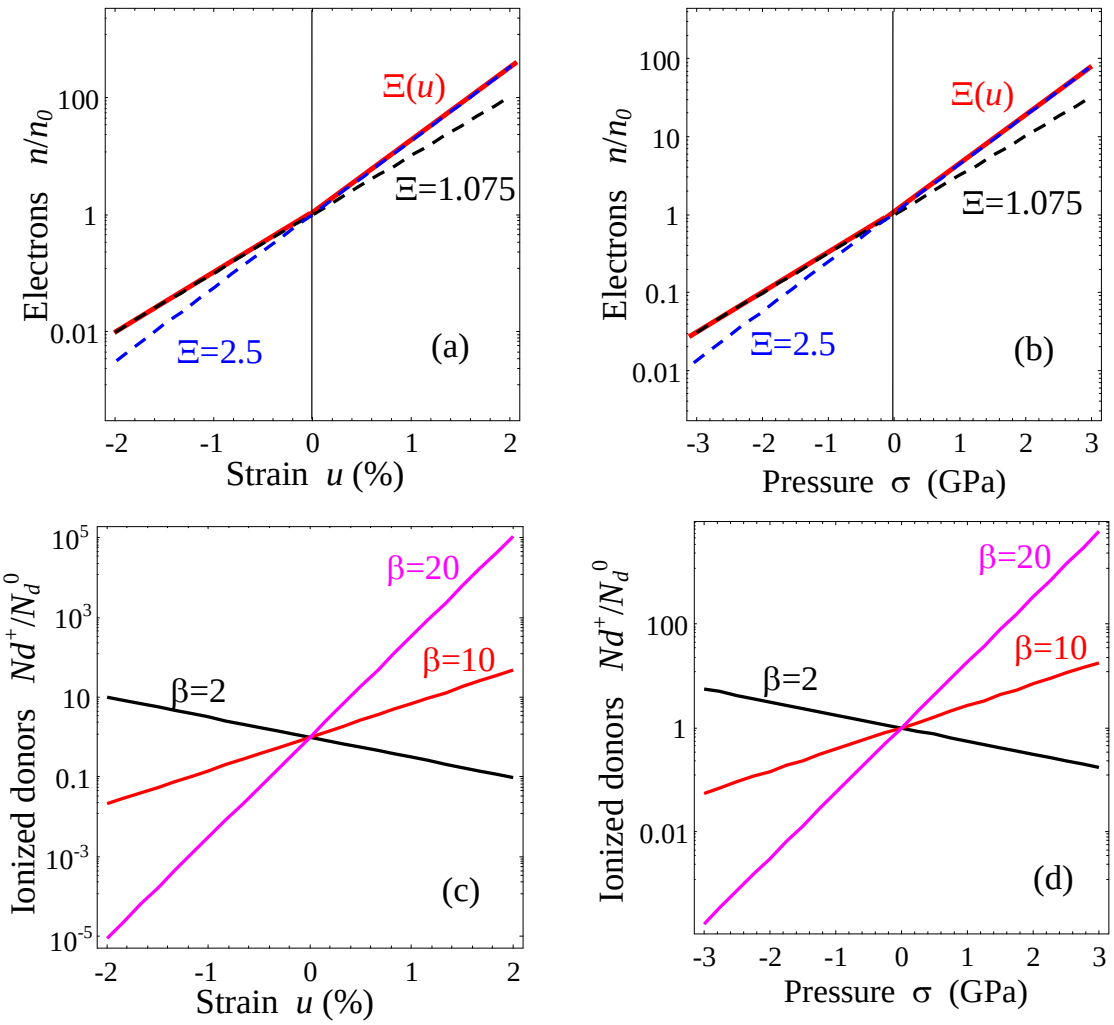

Figure S8. Dependence of the (a,b) electron density and (c,d) ionized donors concentration on (a,c) strain and (b,d) applied pressure. Parameters ef_{ii33} = 5 eV, Ξ_{ii}^{C} = 1.075 eV, 2.5 eV, 2.5 eV (labels near the dashed curves at plots a,b), $\Xi_{11}^{C}(u)$ in accordance with Eq. (2) (labels near the curves at plots c,d), $\tilde{\beta}_{ii} = 2$ eV, 10 eV, 20 eV (labels near the curves at plots c,d), $s_{ii} = 5\times10^{-12}$ Pa^{-1}, T=300 K, $\varphi_{ext} = 0$.

A finite element analysis has been addtionally carried out to analyze the defect concentration profile near NiO surface due to applied AFM indentation forces. Followed by Sheldon and Shenoy,[9] the strain energy is incorporated into the thermodynamic potential to include the elastic effect beside electric field effects. The 2D axisymmetric model depicted in Figure S9 depicts the indented domain (following the Hertz contact theory to model the AFM diamond tip/surface interaction) subjected to a bias voltage. The NiO cell depth is considered to be 256 λ (λ is Debye length). Oxygen removal in NiO is the dominating defect formation mechanism:

$$O_O + Ni_{Ni} \leftrightarrows V_{\ddot{O}} + Ni_{Ni''} + \frac{1}{2}O_2 \qquad \text{(Eq. S5)}$$

where $V_{\ddot{O}}$ are oxygen vacancies and $Ni_{Ni''}$ is Ni^{2+} site receiving two extra electrons. The key feature here is dominant defects with net positive and negative charges denoted by c_v and c_e respectively, representing the defect concentrations (see Ref. 9).

The stress analysis equilibrium equation coupled with the defects induced strains due to volume change are as follows:

$$\nabla \cdot \sigma = 0 \qquad \text{(Eq. S6)}$$

$$\sigma = C : (\varepsilon - \varepsilon_{defect}),\ \varepsilon = \frac{1}{2}[(\nabla u)^T + \nabla u], \qquad \text{(Eq. S7)}$$

$$\varepsilon_{defect} = \frac{1}{3V_m}\{\overline{V_v}[c_v(r,z) - c_v^{\infty}] + \overline{V_e}[c_e(r,z) - c_e^{\infty}]$$

where $c_v^{\infty} = c_e^{\infty}$ are defect concentrations in bulk.

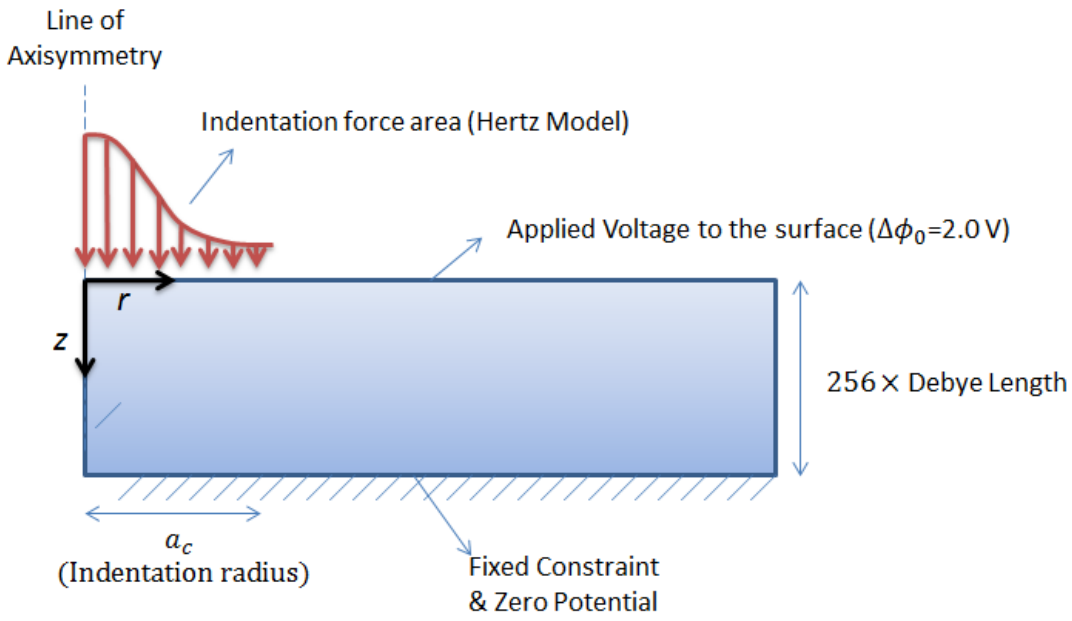

Figure S9.Schametic diagram of the model.

c_v and c_e are defined as:

$$c_v(r,z) = c_v^{\infty} \exp\{\frac{\overline{V_v}}{3RT}[\sigma_r(r,z)+\sigma_\theta(r,z)+\sigma_z(r,z)]\}\exp\{\frac{-2F}{RT}\Delta\phi(r,z)\} \quad \text{(Eq. S8)}$$

$$c_e(r,z) = c_e^{\infty} \exp\{\frac{\overline{V_e}}{3RT}[\sigma_r(r,z)+\sigma_\theta(r,z)+\sigma_z(r,z)]\}\exp\{\frac{+2F}{RT}\Delta\phi(r,z)\}$$

where $\Delta\phi(r,z) = \phi(r,z) - \phi^{\infty}$, $\Delta\phi(r,0) = \Delta\phi_0$.

Then, the potential difference across the space charge layer can be evaluated by solving the Poisson-Boltzmann equation, given in three dimensions by:

$$\nabla^2\Delta\phi = -\frac{F}{\varepsilon_r\varepsilon_0 V_m}[2c_v(r,z) - 2c_e(r,z)] \quad \text{(Eq. S9)}$$

The normalized defect concentrations are defined below:

$$\hat{c}_v = \frac{c_v}{c_v^{\infty}},\ \hat{c}_e = \frac{c_e}{c_e^{\infty}} \quad \text{(Eq. S10)}$$

The indentation distributed pressure using the Hertz theory is applied as boundary condition. Analysis has been done for different scaled values of the indentation force F_i (by keeping the original value of indentation contact radius a_c).

Some other factors such as β and Debye length λ are defined as:

$$\beta = \frac{\overline{V_v}}{\overline{V_O}},\ \lambda = \frac{\sqrt{\varepsilon_r \varepsilon_0 V_m RT}}{2F} \qquad \text{(Eq. S11)}$$

Knowing $\overline{V_v}$ and β, $\overline{V_e}$ is determined using the following stoichiometric relation:

$$\overline{V_O} = -\overline{V_v} - \overline{V_e} \qquad \text{(Eq. S12)}$$

The Hertzian pressure distribution, representing the AFM diamond tip indentation force, on the surface gives:

$$p(r,0) = p_0\left(1 - \frac{r^2}{a_c^{\,2}}\right)^{0.5} \quad (r \le a_c) \qquad \text{(Eq. S13)}$$

where the maximum pressure p_0 is:

$$p_0 = \frac{2E^* a_c}{\pi R_i}. \qquad \text{(Eq. S14)}$$

The indentation radius (contact area radius) a_c terms of the indentation force F_i and the spherical indenter tip radius R_i is calculated from:

$$a_c = \left(\frac{3F_i R_i}{4E^*}\right)^{1/3} \qquad \text{(Eq. S15)}$$

The effective Young's modulus E^* is calculated in terms of indenter tip Young's modulus and poisson's ratio E_i and v_i and the main body's properties E_m and v_m:

$$E^* = \frac{E_i E_m}{E_i(1 - v_m^2) + E_m(1 - v_i^2)}\ . \qquad \text{(Eq. S16)}$$

Table 1. List of Parameters used for finite element modeling

Parameter	Definition	Value	Comments
F_i	Indentation force	3 μN	Assumed
R_i	Indenter tip radius	70 nm	Ref. 10
E_m	Young's modulus of NiO	169 GPa	Refs. 11,12
E_i	Young's modulus of indenter tip	180 MPa	Ref. 13
ν_m	NiO Poisson's ratio	0.3	Refs. 11,12
ν_i	Indenter tip Poisson's ratio	0.28	Ref. 13
c_v^∞	Bulk oxygen vacancy concentration	0.01	Assumed
V_v	Partial molar volumes for extra electron	8.19 cm^3/mol	Assumed
V_m	Molar volume of stoichiometric NiO	11.198 cm^3/mol	Calculated
ε_r	The relative dielectric permittivity of NiO	11.75	Ref. 14
T	Temperature	300 K	From literature
β	See Eq. S11	2.7	Assumed
$\Delta\phi_0$	Fixed surface potential	-2.0 V	Assumed

REFERENCES

1. Choi, J. S.; Kim, J. S.; Hwang, I. R.; Hong, S. H.; Jeon, S. H.; Kang, S. O.; Park, B. H.; Kim, D. C.; Lee, M. J.; Seo, S. *Appl Phys Lett* **2009,** 95, (2) 022109.
2. Kim, K. M.; Jeong, D. S.; Hwang, C. S. *Nanotechnology* **2011,** 22, (25) 254002.
3. Sawa, A. *Mater Today* **2008,** 11, (6), 28-36.
4. Waser, R.; Aono, M. *Nat Mater* **2007,** 6, (11), 833-840.
5. Baytekin, H. T.; Patashinski, A. Z.; Branicki, M.; Baytekin, B.; Soh, S.; Grzybowski, B. A. *Science* **2011,** 333, (6040), 308-312.
6. Kim, Y.; Bae, C.; Ryu, K.; Ko, H.; Kim, Y. K.; Hong, S.; Shin, H. *Appl Phys Lett* **2009,** 94, (3) 032907.
7. Morozovska, A. N.; Eliseev, E. A.; Svechnikov, G. S.; Kalinin, S. V. *Phys Rev B* **2011,** 84, (4) 045402.
8. Bir, G. L.; Pikus, G. E., *Symmetry and Strain-induced Effects in Semiconductors*. Wiley/Halsted Press: 1974.
9. Sheldon, B. W.; Shenoy, V. B., Space charge induced Surface Stresses: Implications in Ceria and Other Ionic Solids. *Phys. Rev. Lett.* **2011**, 106, 216104.
10. http://www.ntmdttips.com/usa/dcp20-15.html
11. Every, A. G. & A. K. McCurdy, in 1.2.1 Elastic constants s, c, edited by Nelson, D. F., Vol. 29a.
12. Plessis, P. de V. Du, Tonder, S. J. van, & Alberts, L., Elastic constants of a NiO single crystal: I (Magnetic transitions). *J. Phys. C: Solid State Phys.* **1971**, 4, 1983.
13. Bharat, B., Kwak, K. J., & Manuel, J., Nanotribology and nanomechanics of AFM probe-based data recording technology. *J. Phys.: Condens. Matter* **2008**, 20, 365207.
14. Gielisse, P. J., Plendl, J. N., Mansur, L. C., Marshall, R., Mitra, S. S., Mykolajewycz, R., & Smakula, A., Infrared properties of NiO and CoO and their mixed crystals. *J. Appl. Phys.* **1965**, 36, 2446-2450.